Rapid Communications

Microscopic mechanism of room-temperature superconductivity in compressed LaH_{10}

Liangliang Liu,[1,2] Chongze Wang,[1] Seho Yi,[1] Kun Woo Kim,[3] Jaeyong Kim,[1] and Jun-Hyung Cho[1,*]

[1]*Department of Physics, Research Institute for Natural Science, and HYU-HPSTAR-CIS High Pressure Research Center, Hanyang University, 222 Wangsimni-ro, Seongdong-Ku, Seoul 04763, Republic of Korea*

[2]*Key Laboratory for Special Functional Materials of Ministry of Education, Henan University, Kaifeng 475004, People's Republic of China*

[3]*Center for Theoretical Physics of Complex Systems, Institute for Basic Science, Daejeon 34051, Republic of Korea*

(Received 11 November 2018; revised manuscript received 22 March 2019; published 4 April 2019)

Room-temperature superconductivity has been one of the most challenging subjects in modern physics. Recent experiments reported that lanthanum hydride $LaH_{10\pm x}$ ($x < 1$) raises a superconducting transition temperature T_c up to ∼260 (or 250) K at high pressures around 190 (170) GPa. Here, based on first-principles calculations, we reveal that compressed LaH_{10} has symmetry-protected Dirac-nodal-line states, which split into holelike and electronlike bands at the high-symmetry points near the Fermi energy (E_F), thereby producing a van Hove singularity (vHs). The crystalline symmetry and the band topology around the high-symmetry points near E_F are thus demonstrated to be important for room-temperature superconductivity. Further, we identify that the electronic states at the vHs are composed of strongly hybridized La f and H s orbitals, giving rise to a peculiar characteristic of electrical charges with anionic La and both anionic and cationic H species. Consequently, a large number of electronic states at the vHs are strongly coupled to the H-derived high-frequency phonon modes that are induced via the unusual, intricate bonding network of LaH_{10}, therefore yielding a high T_c. Our findings elucidate the microscopic mechanism of the observed high-T_c BCS-type superconductivity in LaH_{10}, which can be generic to another recently observed high-T_c hydride H_3S.

DOI: 10.1103/PhysRevB.99.140501

Ever since the first discovery of superconductivity (SC) in 1911 [1], scientists have searched for materials that can conduct electricity without resistance below a superconducting transition temperature T_c. So far, tremendous efforts have been devoted to exploring high-T_c SC in a variety of materials such as cuprates [2], pnictides [3], and hydrogen-rich compounds (called hydrides) [4–7]. Among them, SC in hydrides has been successfully explained by the Bardeen-Cooper-Schrieffer (BCS) theory [8], where SC is driven by a condensate of electron pairs, so-called Cooper pairs, due to electron-phonon interactions. The pioneering idea that hydrogen can be a good candidate for high-T_c SC was proposed by Ashcroft [9], i.e., metallic hydrogen with light atomic mass is expected to have high vibrational frequencies, thereby providing a high T_c due to a strong electron-phonon coupling (EPC). However, the metallization of hydrogen is very difficult to achieve experimentally, because it requires too high pressures over ∼400 GPa [10–12]. Instead, high-T_c SC in hydrides can be realized at relatively lower pressures that are currently accessible using static compression techniques [13]. Motivated by theoretical predictions of high-T_c SC in many hydrides [6,14–16], experiments were performed to confirm that compressed sulfur hydride H_3S exhibits a T_c of 203 K at pressures around 150 GPa [17]. Recently, x-ray diffraction and optical studies demonstrated that lanthanum (La) hydrides can be synthesized in an fcc lattice at ∼170 GPa upon heating to ∼1000 K [18], consistent with the earlier predicted cubic metallic phase of LaH_{10} having cages of 32 H atoms surrounding an La atom [see Fig. 1(a)] [6,7]. Subsequently, two experimental groups nearly simultaneously reported that such an La hydride $LaH_{10\pm x}$ ($x < 1$) exhibits a high $T_c \approx 260$ K at pressures of ∼190 GPa or 250 K at ∼170 GPa [19–23]. Although this observed room-temperature SC in $LaH_{10\pm x}$ has been explained in terms of conventional superconductivity described by the BCS theory [6,7], a microscopic understanding of why LaH_{10} features a strong EPC is still missing.

To explore the microscopic mechanism of the high-temperature BCS-type SC in compressed LaH_{10}, we here, based on first-principles calculations, not only investigate the salient characteristics of electronic, bonding, and phononic properties, but also identify which electronic states are coupled with H-derived high-frequency phonon modes. We reveal that LaH_{10} has symmetry-protected topological Dirac-nodal-line (DNL) states including seven one-dimensional (1D) dispersive nodal lines around E_F. Remarkably, four DNLs split into holelike and electronlike bands at the four equivalent high-symmetry L points on the Brillouin zone boundary near E_F, creating a vHs. The resulting significant increase in the electronic density of states at E_F, which is the key ingredient for room-temperature SC, can thus originate from the crystalline symmetry and the band topology around the high-symmetry points. We further find that the electronic states near E_F exhibit a strong hybridization of the La $4f$ and H s orbitals, giving rise to a peculiar electrical charge characteristic of anionic La and both anionic H_1 and cationic H_2 atoms. This unusual, intricate bonding network of LaH_{10} with the La-H_1 covalent bonds induces the high-frequency vibrations of H atoms, which are, in turn, strongly coupled to large numbers of hybridized La f and H_1 s electronic states at the vHs. The resulting strong EPC significantly enhances T_c, as measured by recent experiments [19–21]. Therefore, our findings shed

*Corresponding author: chojh@hanyang.ac.kr

 ©2019 American Physical Society

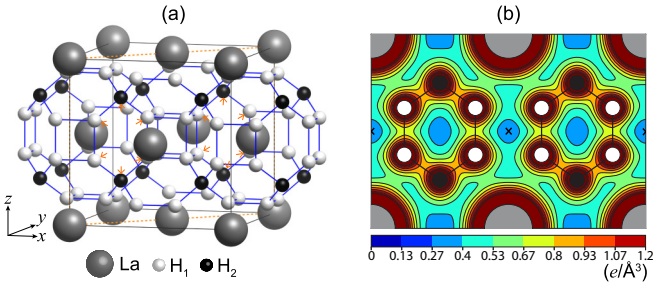

FIG. 1. (a) Optimized structure of the fcc LaH_{10} crystal. The dashed line represents the $(1\bar{1}0)$ face. The H atoms located on the $(1\bar{1}0)$ face are indicated by the arrows. (b) Total charge density ρ_{tot} of LaH_{10}, plotted on the $(1\bar{1}0)$ face. In (b), the contour spacing is 0.13 $e/\text{Å}^3$. The center of the void space surrounded by eight neighboring H_1 atoms is marked "×" in (b).

light on the microscopic mechanism of the high-T_c BCS-type SC observed in compressed LaH_{10}.

Our density-functional theory (DFT) calculations were performed using the Vienna *ab initio* simulation package with the projector augmented-wave method [24–26]. For the exchange-correlation energy, we employed the generalized-gradient approximation functional of Perdew-Burke-Ernzerhof (PBE) [27]. A plane-wave basis was taken with a kinetic energy cutoff of 500 eV. The **k**-space integration was done with $16 \times 16 \times 16$ k points (in the Brillouin zone) for the structure optimization and $70 \times 70 \times 70$ k points for the density of states (DOS) calculation. All atoms were allowed to relax along the calculated forces until all the residual force components were less than 0.005 eV/Å. We construct Wannier representations by projecting the Bloch states from the first-principles calculations of bulk materials onto H s and La s, p, d, and f orbitals, and generate a tight-binding Hamiltonian with a basis of maximally localized Wannier functions [28]. Using the QUANTUM ESPRESSO package [29], we take the $6 \times 6 \times 6$ q points and $24 \times 24 \times 24$ k points for the computation of the phonon frequencies, while the $24 \times 24 \times 24$ q points and $72 \times 72 \times 72$ k points for the EPC constants.

We begin by optimizing the structure of compressed LaH_{10} at 300 GPa using the DFT calculation. Figure 1(a) shows the optimized fcc LaH_{10} structure, which has the lattice parameters $a = b = c = 4.748$ Å. We find that the H_1-H_1 bond length d_1 is 1.145 Å, slightly longer than the H_1-H_2 bond length $d_2 =$ 1.064 Å. These values are in good agreement with those ($d_1 =$ 1.152 Å and $d_2 = 1.071$ Å) of a previous DFT calculation [6] performed at 300 GPa. The calculated total charge density ρ_{tot} of LaH_{10} is displayed in Fig. 1(b). It is seen that H atoms in the H_{32} cage are bonded to each other with covalent bonds. Here, each H-H bond has a saddle point of charge density at its midpoint, similar to the C-C covalent bond in diamond [30]. The charge densities at the midpoints of the H_1-H_1 and H_1-H_2 bonds are 0.74 and 0.91 $e/\text{Å}^3$, respectively. The relatively weaker H_1-H_1 covalent bond is well represented by its larger value of d_1 than d_2. Interestingly, the electrical charges of La and H_1 atoms are connected with each other, indicating a covalent character of the La-H_1 bonds. We note that for other La hydrides such as LaH_{2+x} with fluorite-type structures [31], a charge transfer occurs from La to H atoms, thereby resulting in cationic La and anionic H. But surprisingly, compressed

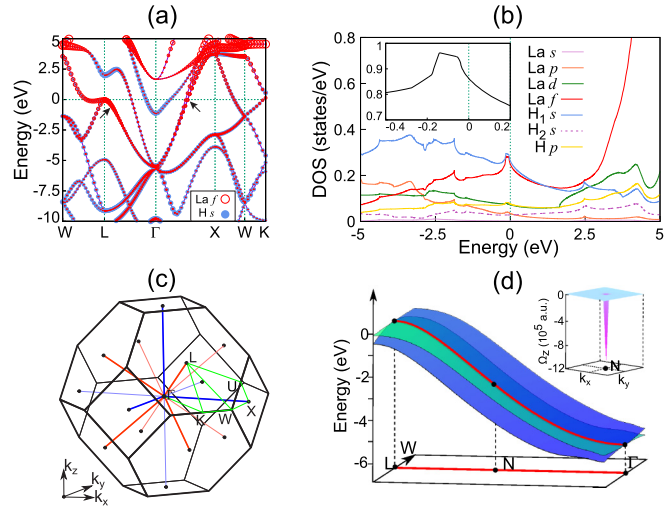

FIG. 2. (a) Calculated band structure and (b) partial DOS of LaH_{10}. In (a), the bands projected onto the H s and La f orbitals are displayed with circles whose radii are proportional to the weights of the corresponding orbitals. The arrows in (a) indicate the DNLs along the $\overline{\Gamma L}$ and $\overline{\Gamma X}$ lines. The energy zero represents E_F. A closeup of the total DOS around the vHs is given in the inset of (b). In (c), all the DNLs along the symmetry-equivalent $\overline{\Gamma L}$ and $\overline{\Gamma X}$ lines are drawn in the first Brillouin zone. The 1D dispersion of the DNL bands along the $\overline{\Gamma L}$ line is displayed in (d), together with the distribution of a Berry curvature component Ω_z around a band touching point N in the DNL.

LaH_{10} is found to exhibit a drastically different feature of electrical charges, i.e., anionic La and both anionic H_1 and cationic H_2, as discussed below. This unusual, intricate bonding network of LaH_{10} contrasts with the previously proposed bonding nature based on a simple charge transfer picture from cationic La to anionic H [7].

Figures 2(a) and 2(b) show the calculated band structure and partial DOS (PDOS) of LaH_{10}, respectively. The band projections onto the H s and La f orbitals are also displayed in Fig. 2(a). Compared to other orbitals, these two orbitals are more dominant components of the electronic states located near E_F (see Fig. S1 of the Supplemental Material [32]). In Fig. 2(a), the band dispersion around the L point (just below E_F) shows the presence of holelike and electronlike bands along the $\overline{LW}$ symmetry line, giving rise to an equal vHs around the four symmetry-equivalent L points [see Fig. 2(c)] in the first Brillouin zone. Using the local principal-axis coordinates, we obtain the effective masses m_1, m_2, and m_3 of the holelike band as $-0.16m_e$, $-1.05m_e$, and $-6.95m_e$ (thermal mass $m_{th} \equiv |m_1 m_2 m_3|^{1/3} = 1.06m_e$), while we obtain those of electronlike band as $-0.09m_e$, $0.79m_e$, and $0.20m_e$ ($m_{th} = 0.24m_e$). Note that the larger the thermal mass, the flatter is the hole- or electronlike band. The inset of Fig. 2(b) displays a closeup of the total DOS around the vHs, which represents the presence of two van Hove singularities separated by $\Delta E_{vHs} \cong 90$ meV. Recently, Quan and Pickett [33] pointed out the importance of such a double-shaped vHs in increasing T_c of compressed H_3S, where the values of m_{th} are $0.42m_e$ and $0.31m_e$ at the two vHs points (with $\Delta E_{vHs} \cong 300$ meV), respectively. We note that the formation of the vHs is associated with the band splitting from the

symmetry-protected DNLs at the high-symmetry points, as discussed below. Thus, the two recently observed high-T_c hydrides, H_3S [17] and LaH_{10} [19,20], have similar electronic features such as DNLs and double-shaped vHs (see Fig. S2 of the Supplemental Material), which can be rather generic to high-T_c superconductivity. It is noteworthy that high-symmetry metallic hydrides having such vHs with large m_{th} can increase their electronic density of states in proportion to the number of equivalent high-symmetry points around which the vHs is created, leading to a strong EPC. Interestingly, the PDOS projected onto the H_1 s and La f orbitals exhibits sharp peaks close to E_F [see Fig. 2(b)], indicating a strong hybridization of the two orbitals. Compared to the H_1 s orbital, the PDOS projected onto the H_2 s orbital is much suppressed around E_F. Such different aspects of the H_1 and H_2 s orbitals reflect their opposite charge characters, i.e., anionic H_1 and cationic H_2, which will be manifested below by a charge-density analysis. The same anionic character of La and H_1 atoms is well consistent with the strong hybridization of La f and H_1 s orbitals just below E_F [see Figs. 2(a) and 2(b)] that produces the formation of the La-H_1 covalent bonds [see Fig. 1(b)].

It is remarkable that the holelike and electronlike bands are degenerate at the L point to form a DNL along the $\overline{\Gamma L}$ line, showing the 1D nodal line with a large bandwidth ~6 eV [see Fig. 2(a)]. Here, we emphasize that the holelike and electronlike bands are split from the DNL bands, producing double-shaped vHs close to E_F. Figure 2(c) displays all the DNLs near E_F, which are computed by using the WANNIERTOOLS package [34]. Here, the tight-binding Hamiltonian with maximally localized Wannier functions [28] reproduces well the electronic bands obtained using the DFT calculation (see Fig. S3 of the Supplemental Material). Since the crystalline symmetry of LaH_{10} belongs to the space group $Fm\bar{3}m$ (No. 225) with the point group O_h, there are four and three DNLs along the symmetry-equivalent $\overline{\Gamma L}$ and $\overline{\Gamma X}$ lines [see Fig. 2(c)], respectively. It is noted that along the $\overline{\Gamma L}$ line, the system has threefold rotation symmetry (C_3) and an inversion (P). These spatial symmetries and time (T) reversal symmetry [35,36] allow two-dimensional irreducible symmetry representations to protect the DNL along the $\overline{\Gamma L}$ line. Similarly, the DNL along the $\overline{\Gamma X}$ line is protected by C_4 and PT. As shown in Fig. 2(d), we find that the band touching points along the DNLs exhibit large Berry curvature distributions. To find the topological characterization of the DNLs, we calculate the topological Z_2 index [37], defined as $\zeta_1 = \frac{1}{\pi}\oint_c dk \cdot \mathrm{A}(k)$, along a closed loop encircling any of the DNLs. Here, $\mathrm{A}(k) = -i\langle u_k|\partial_k|u_k\rangle$ is the Berry connection of the related Bloch bands. We obtain $\zeta_1 = 1$ for the DNLs along the $\overline{\Gamma L}$ and $\overline{\Gamma X}$ lines, indicating that they are stable against perturbations without breaking rotational and PT symmetries. Nevertheless, we find that, when the spin-orbit coupling (SOC) is considered, the DNLs are fully gapped with small gaps [38] (see Fig. S4 of the Supplemental Material). Although the largest gap (~125 meV) is located at the L point, the total DOS around the vHs is similar to that obtained from the DFT calculation without including SOC (see Fig. S5 of the Supplemental Material), which may therefore hardly affect T_c of LaH_{10}.

In order to examine the bonding character between the La atoms and the H_{32} cages, we calculate the charge-density difference, defined as $\Delta\rho = \rho_{tot} - \rho_{La} - \rho_H$, where the second and third terms represent the charge densities of the LaH_0 lattice (i.e., LaH_{10} structure without H atoms) and the La_0H_{10} lattice (LaH_{10} structure without La atoms), respectively. Figures 3(a)– 3(c) show ρ_{La}, ρ_H, and $\Delta\rho$, respectively. Obviously, $\Delta\rho$ illustrates that electron charge is transferred from the H_2 atoms as well as the void space [marked "×" region in Fig. 1(b), surrounded by eight neighboring H_1 atoms] to the La and H_1 atoms. Here, charge accumulation is also seen in the regions between La and H_1 atoms, leading to their covalent bonding character. It is thus likely that the La and H_1 atoms are characterized as being anionic, while the H_2 atoms as being cationic. Such charge characters of LaH_{10} contrast with other La hydrides [31] that comprise cationic La and anionic H atoms. This drastic difference between LaH_{10} and other La hydrides can be ascribed to their different locations of H s orbitals. For LaH_{2+x} with fluorite-type structures [31], the H s orbital is located deeper than the La d or f orbitals, therefore inducing a charge transfer from La to H atoms. Meanwhile, as shown in Figs. 2(b) and 3(e), the PDOS of LaH_{10} and the La_0H_{10} lattice indicates that near E_F, the s orbital of anionic H_1 is more dominant than that of cationic H_2. Consequently, in LaH_{10}, the former s orbital hybridizes quite strongly with the La f orbitals to produce their PDOS peaks near E_F [see Fig. 2(b)]. The charge characteristics of anionic La/H_1 and cationic H_2 with the La-H_1 covalent bonds are found to induce higher phonon frequencies of H_1 atoms compared to H_2 atoms, as demonstrated below. We also find that the frequencies of the Γ-phonon modes in the La_0H_{10} lattice without La atoms are much reduced, compared to those in LaH_{10} (see Fig. S6 of the Supplemental Material).

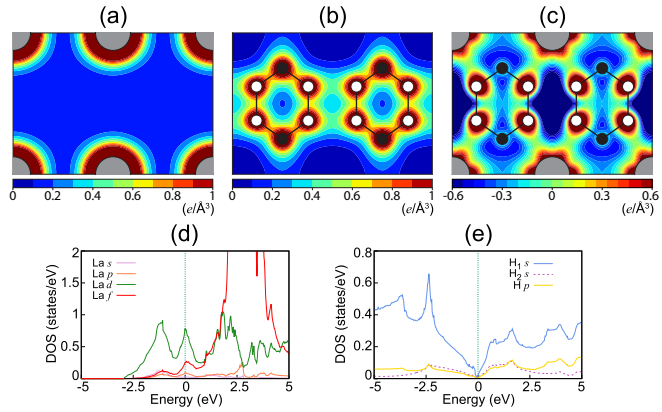

FIG. 3. Calculated charge densities of (a) ρ_{La} and (b) ρ_H in the LaH_0 lattice and the La_0H_{10} lattice, respectively. The charge-density difference $\Delta\rho$ (defined in the text) is displayed in (c). The corresponding partial DOS of the LaH_0 and La_0H_{10} lattices are given in (d) and (e), respectively.

It has been known that the existence of vHs near E_F plays an important role in the BCS-type superconductivity [39–41]. To investigate how the electronic states around the vHs points are strongly coupled to phonon modes, we calculate the phononic properties of LaH_{10}. Figure 4(a) shows the calculated phonon spectrum with the EPC strength, the phonon DOS projected onto selected atoms, and the Eliashberg function $\alpha^2F(\omega)$ with the integrated EPC constant $\lambda(\omega)$. Our

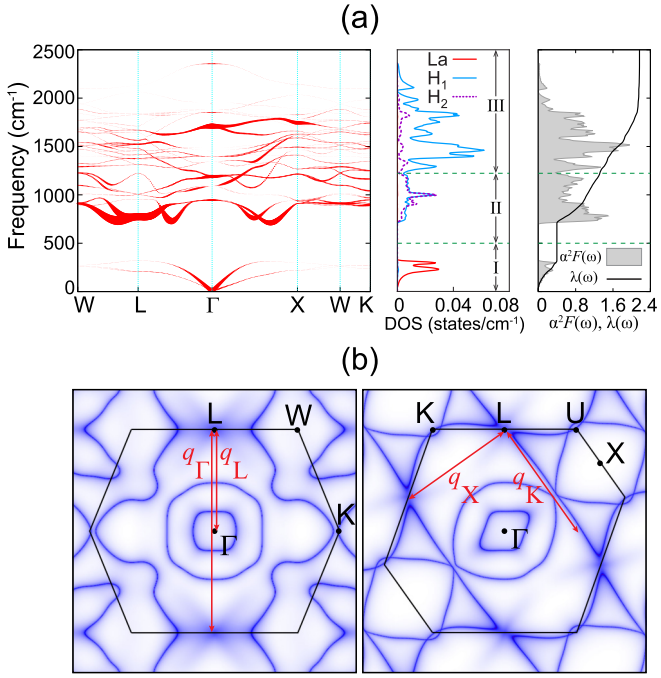

FIG. 4. (a) Calculated phonon spectrum, phonon DOS projected onto selected atoms, Eliashberg function $\alpha^2F(\omega)$, and integrated EPC constant $\lambda(\omega)$ of LaH_{10}. The size of circles on the phonon dispersion is proportional to the EPC strength. In (b), Fermi surface obtained using WANNIERTOOLS [34] is displayed on two different 2D cross sections of the Brillouin zone. Here, the coupling vectors of the vHs points and the Fermi surface are indicated by the double-headed arrows.

results for the phonon dispersion and EPC strength are in good agreement with those obtained by a previous DFT calculation [6]. Interestingly, the phonon DOS is found to be divided into three regions I, II, and III [see Fig. 4(a)]. Here, region I is mostly contributed by the vibrations of La atoms, region II is due to a nearly equal mixture of vibrations from H_1 and H_2 atoms, and region III arises mainly from the vibrations of H_1 atoms. Therefore, we estimate that the optical phonon modes of H_1 atoms contribute to ~62% of $\lambda(\omega)$, while the acoustic (optical) phonon modes of La (H_2) atoms contribute to ~18% (20%) of $\lambda(\omega)$. This estimation indicates that H_1-derived high-frequency optical phonon modes comprise a strong EPC with the electronic states at the vHs, substantially contributing to enhance T_c. We note that the frequencies of whole optical modes range between ~710 and ~2350 cm^{-1}, which are relatively higher than those (500–2000 cm^{-1}) of compressed H_3S [42]. By numerically solving the Eliashberg equations [43] with the typical Coulomb pseudopotential parameter of $\mu^* = 0.13$ [6,7], we estimate $T_c \approx 255$ K (see Fig. S7 of the Supplemental Material), which is much larger than that (~170 K) obtained using the Allen-Dynes [44] equation. In order to choose a proper value of μ^* that fits the experimental data of $T_c = 260$ K (measured at 190 GPa [19]), we calculate the dependence of T_c on μ^* using the Eliashberg equations [43]. The results are given in Fig. S7 of the Supplemental Material. We find that $\mu^* = 0.22$ gives $T_c \approx 220$ K at 300 GPa, which can be interpolated to reach the experimental value of $T_c = 260$ K at 190 GPa using the previous theoretical result (see Fig. 7 of Ref. [6]) of T_c versus pressure. Considering that LaH_{10} and H_3S have similar vibrational and electronic features such as the range of high phonon frequencies and the existence of a double-shaped vHs near E_f, we expect that for LaH_{10}, the nonadiabatic effect with the lowest-order vertex corrections as well as the anharmonic effect would influence μ^* and λ conspicuously, as previously shown in H_3S [14,45]. A more accurate description of the high-T_c SC of compressed LaH_{10} including both nuclear quantum motions and anharmonicity will be demanded in future theoretical work. In Fig. 4(a), the size of the circles on the phonon dispersion represents the EPC strength, which indicates that some strong EPCs occur in the Γ, X, L, and K points. The corresponding phonon wave vectors may be associated with the Fermi-surface nesting. In Fig. 4(b), we plot the Fermi surface with the major nesting vectors q_Γ, q_X, q_L, and q_K. Here, q_Γ and q_X match with the spanning vectors between the vHs points around the L points. For q_L and q_K, the electronic states at the vHs points are likely coupled to the Γ-centered, polyhedron-shaped Fermi surface and the flat Fermi-surface portions, respectively, participating in EPC [see Fig. 4(b)]. Therefore, we can say that the coupling vectors between the vHs points and the Fermi surface account for the strong EPCs in the Γ, X, L, and K points.

To conclude, our first-principles calculations for the electronic, bonding, and phononic properties of the compressed fcc-LaH_{10} phase have revealed two features that are of vital importance in increasing T_c of the BCS-type SC. One is the existence of vHs near E_F, which originates from the hole-like and electronlike bands arising from the splitting of the symmetry-protected topological DNL states at the equivalent high-symmetry L points, and the other represents H-derived high vibrational frequencies that are induced via the unusual, intricate bonding network with anionic La and both anionic H_1 and cationic H_2 atoms. These two features cooperate to produce a strong EPC, thereby enhancing T_c in fcc LaH_{10}. We thus demonstrated that the crystalline symmetry, the band topology around the high-symmetry points near E_F, and the peculiar bonding characters play crucial roles in achieving room-temperature SC in LaH_{10}. Remarkably, two recently observed high-T_c hydrides, LaH_{10} and H_3S, have similar electronic, bonding, and phononic characters such as the double-shaped vHs near E_F, the La-H_1 and S-H covalent bonds, and the H-derived high phonon frequencies. For LaH_{10} (H_3S), the electronic states at the vHs, which are mostly composed of hybridized La f and H_1 s (S p and H s) orbitals, effectively soften H-derived high-frequency phonon modes such as the stretching vibrations of the La-H_1 (S-H) covalent bonds, leading to a strong EPC. It is noted that the fcc LaH_{10} phase can be stabilized at higher pressures above ~170 GPa [18], while it is transformed into a lower-symmetry $C2/m$-LaH_{10} phase on decompression below 170 GPa [46]. Because of the disappearance of vHs near E_F in the $C2/m$-LaH_{10} phase [46], its T_c is expected to be lower than that of the fcc LaH_{10} phase. As a matter of fact, recent experiments reported that T_c was observed to be ~215 K at ~150 GPa [21], which is lower than ~260 (250) K at ~190 (170) GPa [19,20]. The present findings not only provided a microscopic understanding of why compressed fcc LaH_{10} features room-temperature SC with a strong EPC, but also will stimulate further research to

explore other room-temperature superconductors from compressed hydrides.

We are grateful to Professor Yanming Ma for his introduction of the present topic. We also thank Professor Y. Jia for his support. This work was supported by the National Research Foundation of Korea (NRF) Grant funded by the Korean Government (Grants No. 2019R1A2C1002975, No. 2016K1A4A3914691, and No. 2015M3D1A1070609). The calculations were performed by the KISTI Supercomputing Center through the Strategic Support Program (Program No. KSC-2018-CRE-0063) for the supercomputing application research and by the High Performance Computational Center of Henan University.

L.L., C.W., and S.Y. contributed equally to this work.

[1] H. K. Onnes, Commun. Phys. Lab. Univ. Leiden **122**, 124 (1911).
[2] E. H. da Silva Neto, P. Aynajian, A. Frano, R. Comin, E. Schierle, E. Weschke, A. Gyenis, J. Wen, J. Schneeloch, Z. Xu, S. Ono, G. Gu, M. L. Tacon, and A. Yazdani, Science **343**, 393 (2014).
[3] Q. Si, R. Yu, and E. Abrahams, Nat. Rev. Mater. **1**, 16017 (2016).
[4] K. Tanaka, J. S. Tse, and H. Liu, Phys. Rev. B **96**, 100502(R) (2017).
[5] J. P. Carbotte, E. J. Nicol, and T. Timusk, Phys. Rev. Lett. **121**, 047002 (2018).
[6] H. Liu, I. I. Naumov, R. Hoffmann, N. W. Ashcroft, and R. J. Hemley, Proc. Natl. Acad. Sci. USA **114**, 6990 (2017).
[7] F. Peng, Y. Sun, C. J. Pickard, R. J. Needs, Q. Wu, and Y. Ma, Phys. Rev. Lett. **119**, 107001 (2017).
[8] J. Bardeen, L. N. Cooper, and J. R. Schrieffer, Phys. Rev. **106**, 162 (1957).
[9] N. W. Ashcroft, Phys. Rev. Lett. **21**, 1748 (1968).
[10] J. McMinis, R. C. Clay, D. Lee, and M. A. Morales, Phys. Rev. Lett. **114**, 105305 (2015).
[11] J. M. McMahon, M. A. Morales, C. Pierleoni, and D. M. Ceperley, Rev. Mod. Phys. **84**, 1607 (2012).
[12] R. P. Dias and I. F. Silvera, Science **355**, 715 (2017).
[13] N. W. Ashcroft, Phys. Rev. Lett. **92**, 187002 (2004).
[14] I. Errea, M. Calandra, C. J. Pickard, J. Nelson, R. J. Needs, Y. Li, H. Liu, Y. Zhang, Y. Ma, and F. Mauri, Phys. Rev. Lett. **114**, 157004 (2015).
[15] D. V. Semenok, I. A. Kruglov, A. G. Kvashnin, and A. R. Oganov, arXiv:1806.00865.
[16] T. Bi, N. Zarifi, T. Terpstra, and E. Zurek, *Reference Module in Chemistry, Molecular Sciences and Chemical Engineering* (Elsevier, Amsterdam, 2019).
[17] A. P. Drozdov, M. I. Eremets, I. A. Troyan, V. Ksenofontov, and S. I. Shylin, Nature (London) **525**, 73 (2015).
[18] Z. M. Geballe, H. Liu, A. K. Mishra, M. Ahart, M. Somayazulu, Y. Meng, M. Baldini, and R. J. Hemley, Angew. Chem., Int. Ed. **57**, 688 (2018).
[19] M. Somayazulu, M. Ahart, A. K. Mishra, Z. M. Geballe, M. Baldini, Y. Meng, V. V. Struzhkin, and R. J. Hemley, Phys. Rev. Lett. **122**, 027001 (2019).
[20] A. P. Drozdov, P. P. Kong, V. S. Minkov, S. P. Besedin, M. A. Kuzovnikov, S. Mozaffari, L. Balicas, F. Balakirev, D. Graf, V. B. Prakapenka, E. Greenberg, D. A. Knyazev, M. Tkacz, and M. I. Eremets, arXiv:1812.01561.
[21] A. P. Drozdov, V. S. Minkov, S. P. Besedin, P. P. Kong, M. A. Kuzovnikov, D. A. Knyazev, and M. I. Eremets, arXiv:1808.07039.
[22] D. Castelvecchi, Nature (London) **565**, 12 (2018).
[23] E. Zurek, Physics **12**, 1 (2019).
[24] G. Kresse and J. Hafner, Phys. Rev. B **48**, 13115 (1993).
[25] G. Kresse and J. Furthmüller, Comput. Mater. Sci. **6**, 15 (1996).
[26] P. E. Blöchl, Phys. Rev. B **50**, 17953 (1994).
[27] J. P. Perdew, K. Burke, and M. Ernzerhof, Phys. Rev. Lett. **77**, 3865 (1996); **78**, 1396 (1997).
[28] A. A. Mostofi, J. R. Yates, Y.-S. Lee, I. Souza, D. Vanderbilt, and N. Marzari, Comput. Phys. Commun. **178**, 685 (2008).
[29] P. Giannozzi, S. Baroni, N. Bonini, M. Calandra, R. Car, C. Cavazzoni, D. Ceresoli, G. L. Chiarotti, M. Cococcioni, I. Dabo *et al.*, J. Phys.: Condens. Matter **21**, 395502 (2009).
[30] E. Kaxiras, *Atomic and Electronic Structure of Solids* (Cambridge University Press, New York, 2003).
[31] H. Mizoguchi, M. Okunaka, M. Kitano, S. Matsuishi, T. Yokoyama, and H. Hosono, Inorg. Chem. **55**, 8833 (2016).
[32] See Supplemental Material at http://link.aps.org/supplemental/10.1103/PhysRevB.99.140501 for the band projections onto all the H and La orbitals, the electronic bands obtained using the tight-binding Hamiltonian with maximally localized Wannier functions, the frequencies of the Γ-phonon modes in the La_0H_{10}, the band structure and DOS obtained with the inclusion of SOC, together with the results of band structure, PDOS, DNLs, and Berry curvature in H_3S.
[33] Y. Quan and W. E. Pickett, Phys. Rev. B **93**, 104526 (2016).
[34] Q. Wu, S. Zhang, H.-F. Song, M. Troyer, and A. A. Soluyanov, Comput. Phys. Commun. **224**, 405 (2018).
[35] K. Kim, J. Seo, E. Lee, K. T. Ko, B. S. Kim, B. G. Jang, J. M. Ok, J. Lee, Y. J. Jo, W. Kang, J. H. Shim, C. Kim, H. W. Yeom, B. I. Min, B. J. Yang, and J. S. Kim, Nat. Mater. **17**, 794 (2018).
[36] T. Kawakami and X. Hu, Phys. Rev. B **96**, 235307 (2017).
[37] C. Fang, H. Weng, X. Dai, and Z. Fang, Chin. Phys. B **25**, 117106 (2016).
[38] D. Shao, T. Chen, Q. Gu, Z. Guo, P. Lu, J. Sun, L. Sheng, and D. Xing, Sci. Rep. **8**, 1467 (2018).
[39] R. J. Radtke and M. R. Norman, Phys. Rev. B **50**, 9554 (1994).
[40] W. Sano, T. Koretsune, T. Tadano, R. Akashi, and R. Arita, Phys. Rev. B **93**, 094525 (2016).
[41] D. Fang, X. Shi, Z. Du, P. Richard, H. Yang, X. X. Wu, P. Zhang, T. Qian, X. Ding, Z. Wang, T. K. Kim, M. Hoesch, A. Wang, X. Chen, J. Hu, H. Ding, and H.-H. Wen, Phys. Rev. B **92**, 144513 (2015).
[42] D. Duan, Y. Liu, F. Tian, D. Li, X. Huang, Z. Zhao, H. Yu, B. Liu, W. Tian, and T. Cui, Sci. Rep. **4**, 6968 (2014).
[43] G. M. Eliashberg, Zh. Eksp. Teor. Fiz. **38**, 966 (1960) [Sov. Phys. JETP **11**, 696 (1960)].
[44] P. B. Allen and R. C. Dynes, Phys. Rev. B **12**, 905 (1975).
[45] A. P. Durajski, Sci. Rep. **6**, 38570 (2016).
[46] H. Liu, I. I. Naumov, Z. M. Geballe, M. Somayazulu, J. S. Tse, and R. J. Hemley, Phys. Rev. B **98**, 100102(R) (2018).